JOURNAL OF SPACECRAFT AND ROCKETS
Vol. 47, No. 4, July–August 2010

Experimental Investigation on Microwave Interference in Full-Scale Solid Rocket Exhaust

Kiyoshi Kinefuchi*
University of Tokyo, Tokyo 113-8656, Japan
and
Ikkoh Funaki,† Toru Shimada,‡ and Takashi Abe§
Japan Aerospace Exploration Agency, Kanagawa 229-8510, Japan

DOI: 10.2514/1.48173

Under certain conditions during rocket flight, ionized exhaust plumes from solid rocket motors may interfere with RF transmission. To understand the relevant physical processes involved in this phenomenon, measurement of microwave attenuation and phase delay caused by rocket exhaust plumes was attempted in a sea-level static firing test for a full-scale solid propellant rocket motor. The measured data were analyzed by comparing them with simulation results for an exhaust plume flowfield. The results revealed that the change in the shock structure in the plume affects the microwave attenuation level, since it significantly affects the plasma density at the measuring location. When the plasma density in the plume is low, the microwaves can penetrate the plume. The plume plasma properties were successfully estimated for that situation in which the numerically calculated attenuation level agreed well with the experimental results. On the other hand, high-density plasma in the plume does not allow penetration. Therefore, microwaves bypass around the plume and the diffraction effect becomes dominant.

Nomenclature

c = speed of light, m/s
d = exhaust plume diameter, m
k_B = Boltzmann constant, J/K
m_e = electron mass, kg
N = heavy-particle number density, m^{-3}
P_c = combustion chamber pressure, MPa
Q_e = electron collision cross section, m^2
T_e = electron temperature, K
V = received microwave voltage during motor firing, V
V_0 = received microwave voltage before motor firing, V
ν_e = electron collision frequency, s^{-1}
ϕ = phase advance, deg
ω = angular microwave frequency, s^{-1}
ω_p = electron plasma frequency, s^{-1}

I. Introduction

EXHAUST plumes of solid propellant rocket motors interfere with microwave transmission, as illustrated in Fig. 1, and such interference can result in the failure of telecommunications, thereby affecting, for example, telemetry, command, or the radar link between the launch vehicle and the ground-based range safety system. This phenomenon has been addressed in many papers [1–6]. The high-density plasma in the high-temperature exhaust of the motor has been considered to be a possible cause for this effect. In general, solid propellant grains include low-ionization-energy elements such as sodium and potassium as impurities that contribute significantly toward high-density plasma generation [7,8]. As a consequence, plume radio frequency (RF) interference caused by solid propellant motors is known to be significant. On the other hand, plume–RF interference is not so significant in the case of liquid propellant rocket engines because of the relatively low plasma density of the exhausts [9].

The current status of technology relevant to dealing with this issue is inadequate in that it is impossible to simulate the plume–RF interference while taking into consideration all the details of the processes involved because of the following reasons:

1) The plume plasma properties that affect RF transmission, obey nonequilibrium ionization processes, including effects due to aluminum and aluminum-oxide particles, alkali metal impurities, and chemical reactions with turbulent mixing. Because such processes are not well understood, an accurate determination of the plasma properties using theoretical solutions is difficult.

2) During rocket flights, the microwave transmission path penetrates the three-dimensional plasma plume and, in addition, diffraction and reflection are also involved.

Numerical calculations that take all these effects into account are not practical, because numerous calculations are required.

For the development of a technique to determine the attenuation level in real flight conditions, it is necessary first of all to understand the essence of the physics underlying the interactions, rather than to study all the details involved in the phenomenon and then develop a detailed RF transmission simulation tool that includes all these details. It is appropriate for this purpose to investigate microwave interactions with the plume in a static firing test, because all the basic interaction mechanisms are included in a simple plume–RF interaction configuration. Also, it is desirable to use a full-scale motor, because the exhaust plume size significantly affects microwave transmission parameters such as plume penetration, diffraction, and reflection; thus, small motors would not be suitable for this purpose.

Hence, in this paper, we investigate microwave transmission behavior in sea-level static firing tests conducted with a full-scale solid rocket motor. We measure microwave attenuation for three frequencies (*S*-band, *C*-band, and *X*-band) and the phase delays by using a simple antenna setup. Flowfield simulations of the exhaust plumes were conducted in order to analyze the experimental results. The mechanisms of plume-microwave interference are discussed taking all these results into account.

Received 18 November 2009; revision received 15 March 2010; accepted for publication 19 March 2010.

*Graduate Student, Department of Aeronautics and Astronautics. Member AIAA.

†Associate Professor, Institute of Space and Astronautical Science. Member AIAA.

‡Professor, Institute of Space and Astronautical Science. Senior Member AIAA.

§Professor, Institute of Space and Astronautical Science; Professor, University of Tokyo. Associate Fellow AIAA.

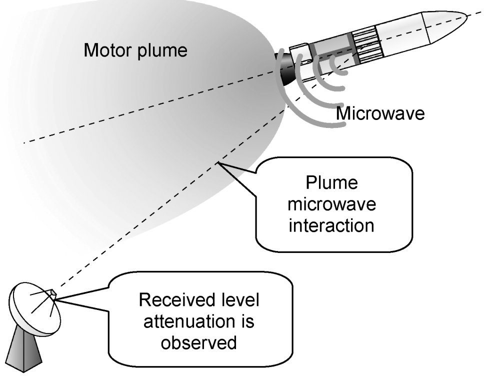

Fig. 1 Plume–RF interaction in rocket flight. The plume from the solid rocket motor impedes microwave transmission.

II. Experimental Setup

Microwave attenuation experiments were conducted during static firing tests with a full-scale solid rocket motor. Three microwave frequencies normally used for space communication were selected: S-band, 2.3 GHz; C-band, 5.6 GHz; and X-band, 8.5 GHz. Horn-type antennas were adopted for both the transmitter and the receiver in order to achieve high directivity. Three-frequency horn-type antennas were assembled (shown in Fig. 2) with thermal insulation for each transmitter and receiver. The main objective of this study is to understand the essence of the interaction so that we adopted simple antenna setup in order to simplify the discussions; that is, the solid motor was located horizontally, and the transmitter and receiver antenna assemblies were placed on the motor test site facing each other across the motor plume, as shown in Fig. 3. The heights of the antennas were adjusted to the motor nozzle center of axis.

Figure 4 shows the microwave attenuation and phase-delay measurement systems. Microwaves of all three frequencies were received and finally downconverted to 10 kHz; they were then recorded on a digital data recorder with a sampling rate of 48 kHz. The attenuation was evaluated as received microwave voltage ratio, V/V_0, by comparing the received microwave voltage before and during the motor firing. In this paper, the term *attenuation* means $1 - (V/V_0)^2$. The error in the voltage ratio is about $\pm 2\%$. For the phase-delay measurement, the S-band signal was divided from the oscillator, and its phase was periodically delayed by using the phase shifter. The phase-delayed signal was mixed with the signal received by the receiver antenna. The mixing was switched on and off at 1 s intervals by using an RF switch for evaluation of both the attenuation and the phase delay. The phase delay corresponds to the output of the phase shifter when the resultant wave reaches the maximum value. The error in the phase delay is somewhat large, about ± 10 deg, mainly because the resultant waveform is relatively flat around the maximum and there is some uncertainty for the determination of the maximum.

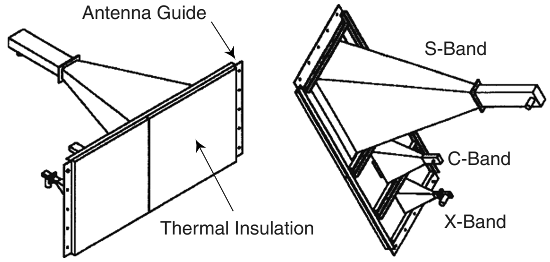

Fig. 2 Antenna assembly. Three horn-type antennas were assembled with thermal insulation.

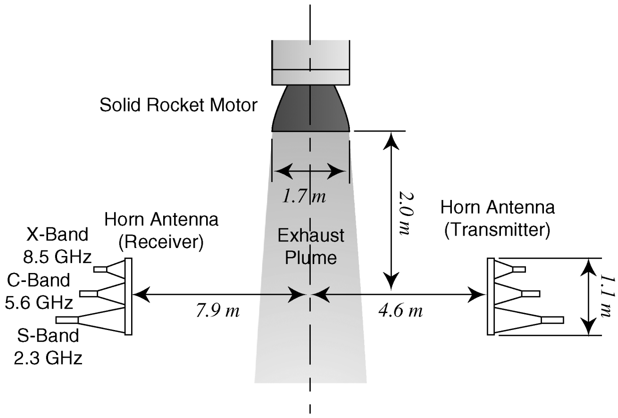

Fig. 3 Antenna setup for the experiments.

III. Numerical Methods and Results

Before discussing the experimental results, it is appropriate to examine the plume flow structure expected in the experiment, because the plasma density distribution in the motor plume depends on the flow structure. Therefore, a numerical simulation code that models the flowfield of solid rocket plumes [10] was employed. In this code, we adopted the axisymmetric Euler equation, because the turbulent mixing effect in the plume would be negligible near the nozzle exit: that is, at the antenna location [11]. The governing equations are spatially discretized by using the finite volume method, and the convective flux is evaluated according to van Leer's flux-vector splitting method. For time integration, the lower-upper symmetric Gauss–Seidel implicit algorithm is used.

Since the physics of solid motor flow is complicated, because of many gas-dynamics and physicochemical processes, we set some assumptions, described and explained as follows. The actual exhaust flowfield of solid propellant rocket motors contains alumina particles in general. Since almost all of the alumina particles are submicron order in size, they immediately follow the speed of the gaseous phase. Thus, we assume that the gaseous and solid phases have achieved equilibrium, thus allowing us to employ the mean properties of combustion gas and alumina particles [10]. Because the molecular weight of the flow is almost the same as that of air, we assume that the fluid properties outside the plume are the same as those within the plume, which allows us to adopt the one-fluid approximation. The calculation model is shown in Fig. 5; in this case, the solid propellant grain surface is outside the calculation region, and the flow rate of the combustion gas is determined from the experimentally measured combustion velocity of the grain. Figure 6 shows the calculation grid, which is 81×54 in the nozzle region and 287×81 in the outer region.

Because the microwave attenuation depends on the plasma density and the electron collision frequency in the plume, we used some assumptions to estimate them. For the ionization reaction and the combustion reaction, it was assumed that chemical equilibrium was established only in the combustion chamber and that the reactions were frozen downstream from the combustion chamber. This assumption for the reactive flow is called the *frozen-flow* approximation and probably valid in the motor nozzle [12]; however, it is still unclear for exhaust plumes and it will be discussed later. Since the combustion temperature strongly affects the electron density, we estimated the actual combustion temperature by using the combustion efficiency obtained from the motor firing test and the theoretical adiabatic temperature. The equilibrium calculation in the combustion chamber was conducted taking into account our solid propellant ingredient, which mainly includes hydroxy-terminated polybutadiene, ammonium perchlorate, and aluminum. For estimating the plasma density, the impurities including sodium and potassium must be taken into account in general, since their ionization potentials are especially low. The grain used in this test, composite propellant, contains no potassium; potassium is generally contained in nitrocellulose that is used in double-base propellants. Here, we considered sodium sulfate (Na_2SO_4) in the propellant. Figure 7 shows an example of the results of the equilibrium calculation for mole fractions of ions and electrons under $P_c = 10$ MPa. The electron

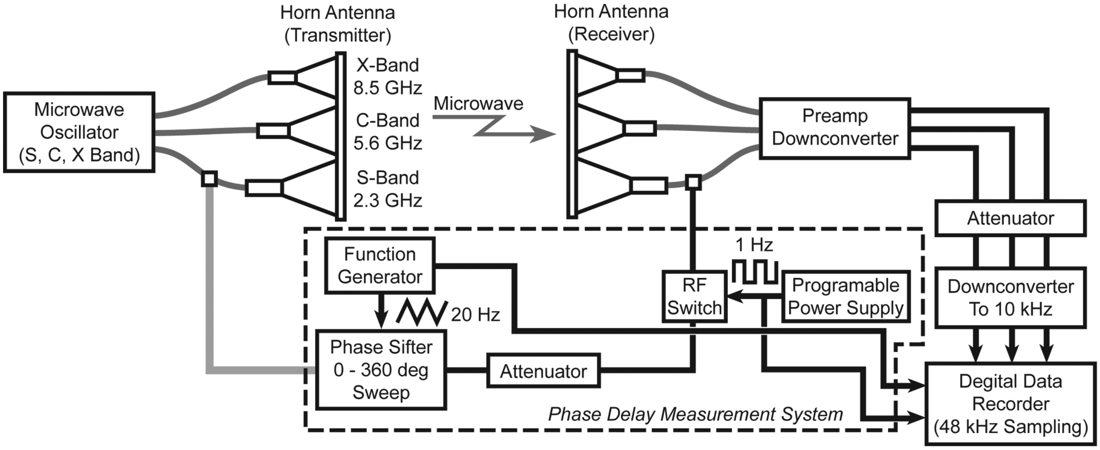

Fig. 4 Microwave attenuation and phase-delay measurement system used in the experiments.

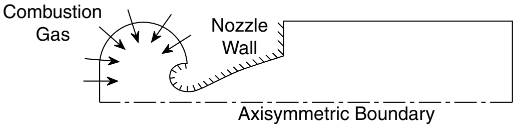

Fig. 5 Computational model for plume flowfield calculations.

mole fraction, or degree of ionization, is 1.59×10^{-7}, and the electron number density in the combustion chamber was estimated to be 3.54×10^{19} m^{-3}. We assumed that the reactions were frozen downstream from the combustion chamber and thus the electron mole fraction was conserved in the entire calculation region. The electron collision frequency can be expressed as follows [11,13]:

$$\nu_e = NQ_e\sqrt{\frac{8k_BT_e}{\pi m_e}} \tag{1}$$

We assumed that the electron temperature and the flow temperature were the same, because thermodynamic equilibrium would be achieved, due to enough collisions between electrons and heavy particles.

The flowfields were calculated for combustion chamber pressure (P_c) values of: 10.0, 8.2, 7.5, 7.0, 6.2, 6.0, and 5.5 MPa. The choice of these combustion pressures was based on the experimental results, described in the next section. It was noted from the video of the plume during the motor firing that the flow separation in the nozzle occurred after the cutoff transition ($P_c < 4$ MPa). Thus, the flow was fully attached to the nozzle wall for all the calculations. Figure 8 shows the calculation results for the plasma density distribution under the frozen-flow approximation. The LOS (line of sight) of the antenna assembly is also shown as a dotted line in the figure. It should be noted that the one-fluid approximation was adopted in our calculation and the frozen-flow plasma density is simply proportional to the flow density. Therefore, the plasma density outside the plume region was set to zero, because the plasma density would appear to be high outside the plume region without this treatment.

Several shock structures in the plume can be seen in Fig. 8. Oblique shock waves or barrel shock waves are observed in all the chamber pressure cases, and a Mach disk (perpendicular shock wave) appears for P_c values of 6.0 and 5.5 MPa. Downstream of these shocks, the plasma density increases because the flow is compressed and heated. The shock structures move upstream and the plasma density on the LOS of the antennas changes with decrease in the chamber pressure. It is also observed in Fig. 8 that the plume diameter on the LOS decreases with decreasing chamber pressure.

IV. Experimental Results and Discussion

A. Basis for the Plume–Microwave Interaction

Under our experimental conditions, there would be two microwave transmission paths: not only the plume penetration path but also the diffraction path, which bypasses the plume by going around it. When the plume penetration path is dominant, the microwave attenuation characteristics depend on the electron plasma frequency ω_p and the electron collision frequency ν_e in the exhaust plume. This characteristic is roughly explained by the plane-wave–slab-plasma interaction theory [14–16], in which it is assumed that plane waves travel through the slab-plasma region and gradually attenuate. In this theory, the following assumptions are made [16]:

1) Uniform plasma in which electrons interact only through collective space charge forces.

2) Ions and neutral molecules are regarded as a continuous stationary fluid through which electrons move with friction.

3) Thermal particle motion can be ignored to assume a cold plasma.

4) There is no magnetic field.

Applying the equation of motion of an electron and Maxwell equations, the relationship between the attenuation and plasma properties (ω_p and ν_e) is derived as follows:

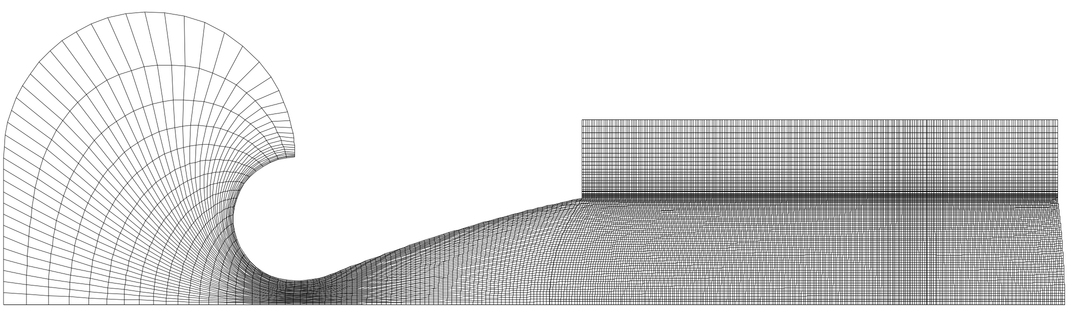

Fig. 6 Computational grid for plume flowfield calculations.

$$\frac{V}{V_0} = \exp\left[-\frac{\omega d}{c}\sqrt{-\frac{1}{2}\left(1-\frac{(\omega_p/\omega)^2}{1+(\nu_e/\omega)^2}\right)+\frac{1}{2}\sqrt{\left(1-\frac{(\omega_p/\omega)^2}{1+(\nu_e/\omega)^2}\right)^2+\left(\frac{(\omega_p/\omega)^2}{1+(\nu_e/\omega)^2}\cdot(\nu_e/\omega)\right)^2}}\right] \quad (2)$$

Equation (2) shows that the high plasma density causes significant microwave attenuation with the attenuation of low-frequency microwaves being more significant. If the penetration of the plume by the microwaves is the dominant path, the attenuation characteristics may be in accordance with this theory. However, if the diffraction path dominates the microwave transmission, the high-frequency microwaves show higher attenuations, in contrast to the situation for the penetration path, because higher frequencies seldom spread out into the region behind the plume, due to its high directivity.

B. Experimental Results and Estimation of Plasma Characteristics

The experimental results are shown in Fig. 9. The combustion chamber pressure of this solid motor gradually decreases with time. Therefore, the received microwave voltage ratios V/V_0 for the three frequencies (not in the decibel scale) and S-band phase delay are plotted against the combustion chamber pressure. The measured voltage ratios for three frequencies were averaged in 1 s intervals in order to reduce the noise generated by the flow turbulence [7]. As can be seen in Fig. 9, there is an apparent relationship between the voltage ratios and the chamber pressure P_c. In addition, lower-frequency microwaves show higher attenuations for $P_c > 5.8$ MPa. This frequency dependence of attenuation corresponds to the characteristics of the plume penetration path expressed by Eq. (2). It is observed that attenuations are the highest below about 5.5 MPa and almost saturate for every frequency and that the dependence on frequency changes. It is possible that the attenuation saturations observed in the experiment correspond to the Mach disk appearance, because the computational fluid dynamics (CFD) results showed that it appears in the $P_c = 5.5$ and 6.0 MPa cases. A large phase delay in the S-band also appears in this combustion pressure region. The dependence on frequency observed in this regime suggests that not only the penetration path, but also the diffraction path, is present. We will discuss this situation later.

By substituting the experimental results of voltage ratios in Eq. (2), ω_p and ν_e in the plume can be estimated when the penetration path is dominant. We adopt voltage ratios of C-band and X-band for the estimates, because it is possible that the S-band takes not only the penetration path but also the diffraction path, as will be explained later. Estimated ω_p and ν_e are shown in Fig. 10 against combustion chamber pressure. Here, we used the nozzle exit diameter as the plume diameter d. This assumption may be rough, because the flowfield simulation results indicate the plume diameter at the antenna position shrinks with decreasing combustion chamber pressure, as shown in Fig. 8. However, this assumption is very useful for the discussion regarding the plasma characteristics in the plume. As seen in Fig. 10, the plasma frequency increases with decreasing chamber

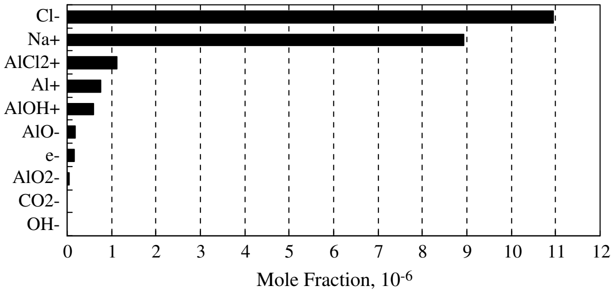

Fig. 7 Mole fractions of ions and electrons in the combustion chamber with $P_c = 10$ MPa. Major elements (10^{-7} or more) are shown.

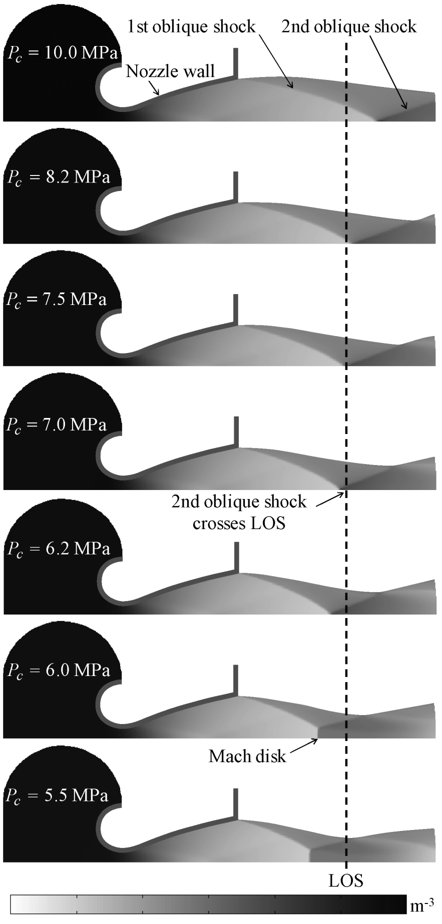

Fig. 8 Plume flowfield calculation results for the frozen-flow plasma density for various chamber pressures.

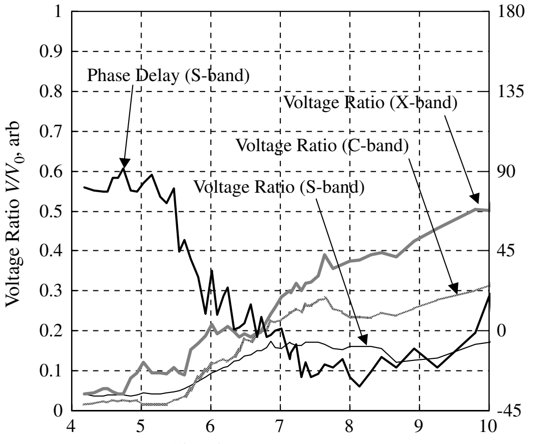

Fig. 9 Experimental results: microwave voltage ratios V/V_0, S-band phase delay against chamber pressure; S-band, 2.3 GHz; C-band, 5.6 GHz; and X-band, 8.5 GHz.

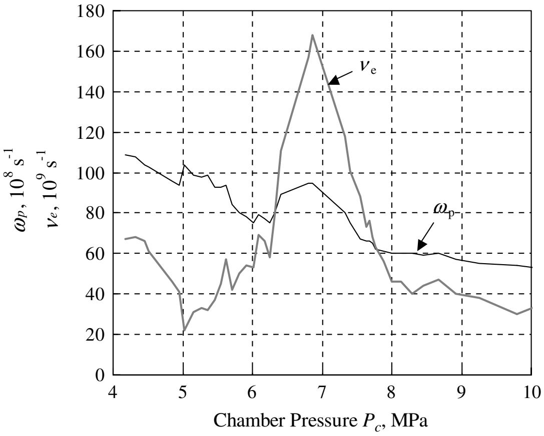

Fig. 10 Estimated plasma frequency and electron collision frequency by using experimental voltage ratios of *C*-band and *X*-band (assuming plume diameter equals the nozzle exit diameter).

pressure. However, the electron collision frequency is seen to be the highest at about 6.9 MPa.

C. Prediction of Microwave Attenuation

The attenuation (voltage ratio) has been predicted using the flowfield calculation results and the plane-wave–slab-plasma interaction theory [Eq. (2)]. Radial variations of the frozen-flow plasma density on the LOS of the antenna assembly for various combustion chamber pressures are shown in Fig. 11. Figure 12 shows the simulated electron collision frequency. The experimentally estimated values (seen in Fig. 10) are also shown in these figures. It should be noted again that the values in Fig. 10 were calculated assuming that the plume diameter equals the nozzle exit diameter.

The simulated plasma density and the collision frequency near the plume core ($r \sim 0$) increase with decreasing combustion pressure until $P_c = 7.0$ MPa, after which, these values decrease with decreasing combustion pressure. This trend agrees with the experimental estimates for the electron collision frequency (maximum at $P_c = 6.9$ MPa, as shown in Fig. 10). However, in regard to the plasma density, this trend does not agree with the experimental data in which the plasma density increases with decreasing chamber pressure, as shown in Fig. 10. This disagreement could be caused by the fact that the flowfield calculations could not successfully simulate plasma density in the high-plasma-density regions, such as downstream of the second oblique shock or the Mach disk. This explanation will be discussed in detail in the next section.

Under the assumption of the slab model, we can estimate the attenuation levels by using these flowfield simulation results. That is, using the values for the plasma density and the collision frequency shown in Figs. 11 and 12 respectively, Eq. (2) gives the attenuation level shown in Fig. 13. The experimental results are also shown in this figure. The calculated result is in agreement with the experimental result when P_c is greater than 7.0 MPa. When P_c is less than 7.0 MPa, the calculated results show larger voltage ratios, i.e., lower attenuation, than the experimental results. In Figs. 11 and 12, when P_c decreases from 7.5 to 7.0 MPa, the plasma density and the collision frequency near the plume core ($r \sim 0$) both rapidly increase. This is because of the appearance of the second oblique shock on the LOS, as also seen in Fig. 8. The underestimation of the attenuations at $P_c < 7.0$ MPa in Fig. 13 means that the plasma densities in the downstream of the second oblique shock and the Mach disk are underestimated in the frozen-flow approximation. The actual plasma density in these regions should be higher than that obtained with the frozen-flow estimation. In the upstream of these shocks, however, our calculation successfully simulated the flowfield and the calculated result was very similar to the experimental result, as shown in Fig. 13.

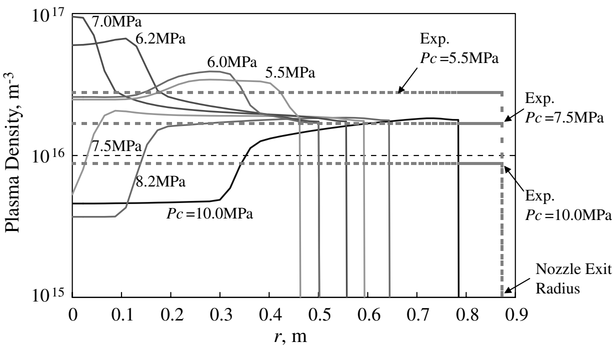

Fig. 11 Radial plasma density distribution on the LOS for various combustion chamber pressures (frozen flow).

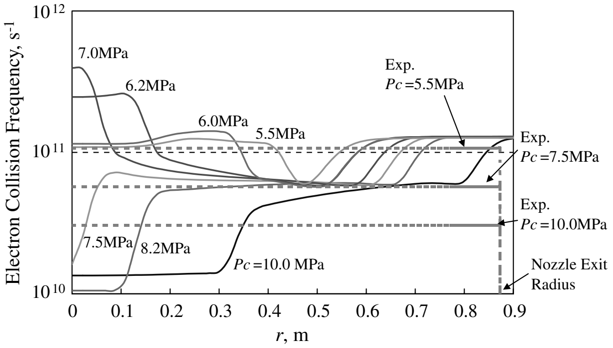

Fig. 12 Radial electron collision frequency distribution on the LOS for various combustion chamber pressures.

D. Downstream of the Second Oblique Shock and the Mach Disk

The plasma density was estimated under the frozen-flow approximation as explained earlier. This approximation is valid only for the high-flow-velocity region, where the flow characteristic time is much shorter than the chemical reaction times. In the downstream of the second oblique shock and the Mach disk, the flow velocity rapidly decreases so the frozen-flow approximation would be no longer valid. Furthermore, gas–particle nonequilibrium and unsteady mixing take place in the downstream of Mach disk [17]. Although these physical processes affect plasma density and electron collision frequency, our simulations do not take them into account. These nonequilibrium and unsteady effects must be considered for accurate plasma density estimation in the downstream of the second oblique shock and the Mach disk. That is why our simulation underestimated the plasma density in these regions. Afterburning in the mixing layer is also important for plasma generation. Afterburning especially grows in the downstream region of the

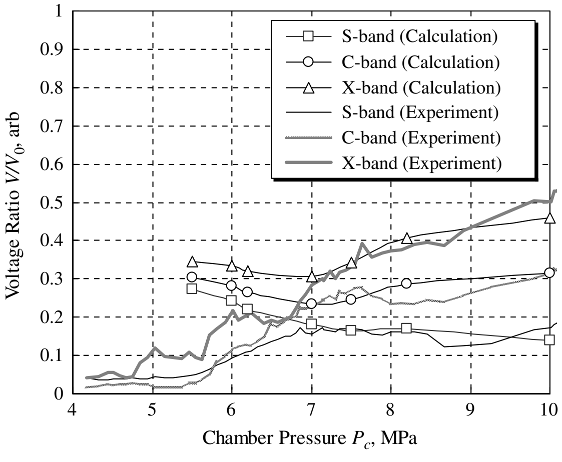

Fig. 13 Comparisons between the calculated and experimentally derived attenuations (voltage ratios). Calculations are based on the frozen-flow CFD results and Eq. (2).

plume [11]. This effect, however, could be neglected in our experiment, because our measurement was conducted near the nozzle exit, where the afterburning layer has not yet grown significantly.

E. Microwave Transmission Characteristics

In the experiment, microwaves reach the receiver antenna after penetration through the plume or diffraction around the plume. The experimental and calculated voltage ratios shown in Fig. 13 agree well before the second oblique shock appearance on the LOS (when $P_c > 7.0$ MPa). The penetration path is dominant in this case, and the plane-wave–slab-plasma theory expressed by Eq. (2) is applicable. The numerical plasma density and the electron collision frequency shown in Figs. 11 and 12 are reliable when $P_c > 7.0$ MPa.

Next, let us consider the microwave transmission mode when $P_c < 7.0$ MPa. We measured the phase delay of the *S*-band signal, as shown in Fig. 9, and observed no phase delay for $P_c > 7.0$ MPa; however, when P_c decreases from 7.0 to 5.5 MPa, the phase delay gradually increases. When $P_c < 5.5$ MPa, the phase delay saturates at about 90 deg. According to the slab-plasma theory, phase advance through plasmas, ϕ in degrees, can be expressed as follows:

$$\phi = \frac{180}{\pi}\frac{\omega d}{c}\left[1 - \sqrt{\frac{1}{2}\left(1 - \frac{(\omega_p/\omega)^2}{1+(\nu_e/\omega)^2}\right) + \frac{1}{2}\sqrt{\left(1 - \frac{(\omega_p/\omega)^2}{1+(\nu_e/\omega)^2}\right)^2 + \left(\frac{(\omega_p/\omega)^2}{1+(\nu_e/\omega)^2}\cdot(\nu_e/\omega)\right)^2}}\,\right] \tag{3}$$

To estimate ϕ, we use the flowfield calculation results (Figs. 11 and 12) and the values obtained from measured attenuation levels (shown in Fig. 10). Comparison of the *S*-band phase delay between the experimental result and the values calculated by Eq. (3) is shown in Fig. 14. In the diffraction-dominant case, microwave bypass around the plume so that the microwave path length to the receiver becomes longer than that of the penetration-dominant case. Because the longer path length corresponds to the larger phase delay, the transmission mode transition from the penetration path to the diffraction path causes the phase delay. For example, when the path length of the *S*-band, whose wavelength is 0.13 m, increases by 0.03 m, about a 90 deg phase delay is observed. On the other hand, the plasma penetration causes the phase advance according to Eq. (3). For P_c greater than 7.0 MPa, the three plots in Fig. 14 show small negative values (phase advance) and good agreement; this implies that the plasma penetration path is dominant for the *S*-band.

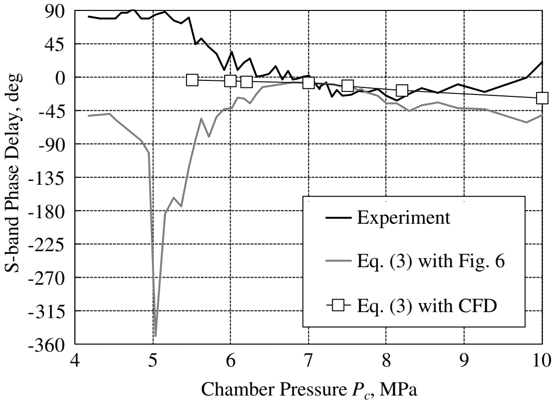

Fig. 14 Comparison of *S*-band phase delays derived experimentally by calculation using Eq. (3) with the CFD result and by calculation using Eq. (3) with the values given in Fig. 6.

However, when P_c is less than 7.0 MPa, a large positive value (phase delay) is observed in the experiment. This indicates that diffraction is dominant for the *S*-band and that most of the *S*-band microwaves cannot penetrate the plume. In the diffraction-dominant case, Eq. (3) is no longer valid, because this equation is derived under the assumption that microwaves completely penetrate the plume. There is a large difference between the calculations, due to the underestimation of the plasma density in CFD, as explained in the above section.

When P_c decreases from 7.0 to 5.5 MPa, the high-plasma-density region in the downstream of the second oblique shock affects the microwave transmission, and the length of this region on the LOS becomes larger with the decreasing combustion pressure, as shown in Fig. 8. Hence, because the length of this region on the LOS corresponds to the diffraction path length, the phase delay increases with decreasing combustion pressure. The phase delay saturates at $P_c < 5.5$ MPa in the experiment, as shown in Fig. 9, because this combustion pressure region would correspond to the existence of the Mach disk when $P_c \leq 6.0$ MPa. It is expected that the diameter of the Mach disk would hardly change with decreasing combustion pressure.

Because the experimental data for $P_c < 5.5$ MPa in Fig. 9 shows that the attenuation is large in the order of *C*-band, *S*-band, and *X*-band, it can be inferred that the *S*-band hardly penetrates the plume while most of the *X*-band still can penetrate it. The *C*-band probably penetrates as well as diffracts. Accordingly, we calculated ω_p and ν_e, as shown in Fig. 10, by using the voltage ratios of only the *C*- and *X*-bands and excluding the *S*-band. The plasma density and the electron collision frequency in $P_c < 5.5$ MPa in Fig. 10 would still have some uncertainty, due to the uncertainties regarding the diffraction effect of the *C*-band.

V. Conclusions

To determine the underlying mechanisms of plume–RF interference, experiments were conducted on the interactions between the rocket exhaust and microwaves during a full-scale solid rocket firing test. The plasma characteristics along the LOS for the microwave transmission were significantly affected by variations in the flowfield structure caused by the variations in the chamber pressure of the motor as suggested by the numerical simulation of the flowfield. When the plasma density in the plume was low (in other words, when the plume penetration path was dominant), the plane-wave–slab-plasma interaction theory was applicable for the evaluation of microwave attenuation, and the plasma characteristics were successfully determined. When the plume had a higher plasma density, microwaves hardly penetrated it and instead bypassed around it; i.e., the diffraction effect became dominant. The diffraction effect changed the microwave path length to the receiver and caused the phase delay. Therefore, because of the diffraction path, some uncertainty is introduced in the estimated plasma density and the electron collision frequency in the high-plasma-density regions is determined by using experimentally measured attenuation data.

Based on the flowfield calculations under the frozen-flow assumption, the plasma distribution in the plume was estimated. The plasma distribution in the low-plasma-density regions gives a reasonable estimate of the attenuation level observed in the experiment. However, in the high-plasma-density regions, such as downstream of the Mach disk or the second oblique shock, the numerical results underestimate the plasma density, because the frozen-flow approximation is no longer valid in such a low-flow-velocity region.

Acknowledgments

This study was supported by many staff members of Japanese rocket motor testing and development. We would like to express our gratitude to all those who contributed to the testing. We are indebted to T. Kato, S. Tachikawa, and H. Ogawa of the Institute of Space and Astronautical Science for their valuable cooperation.

References

[1] Abe, T., Fujita, K., Ogawa, H., and Funaki, I., "Microwave Telemetry Breakdown Caused by Rocket Plume," 31st AIAA Plasmadynamics and Lasers Conference, AIAA Paper 2000-2484. Denver, CO, 2000.

[2] McIver, D. E., Jr., "The Radio Frequency Signal Attenuation Problem of Rocket Exhaust," *Proceedings of the NASA Conference on Communicating Through Plasmas of Atmospheric Entry and Rocket Exhaust*, NASA Langley Research Center, Hampton, VA, 1964, pp. 167–179.

[3] Wood, W. A., and DeMore, J. E., "Microwave Attenuation Characteristics of Solid Propellant Rocket Exhaust Products," AIAA 6th Solid Propellant Rocket Conference, AIAA Paper 65-183, Washington, D.C., 1965.

[4] Vicente, F. A., Taylor, E. C., and Phelps, R. W., "Analysis of Flame Effects on Measured Electromagnetic Propagation Date," *Journal of Spacecraft and Rockets*, Vol. 4, No. 8, 1967, pp. 1069–1075. doi:10.2514/3.29020

[5] Boynton F. P., and Pajasekhar, P. S., "Plume RF Interference Calculations for Space Shuttle," NASA CR-161099, 1978.

[6] Smoot, L. D., "Causes of Ionization in Rocket Exhausts," *Journal of Spacecraft and Rockets*, Vol. 12, No. 3, 1975, pp. 179–183. doi:10.2514/3.27825

[7] Smoot, L. D., and Seliga, T. J., Jr., "Rocket Exhaust Plume Radar Attenuation and Amplitude/Phase Noise," *Journal of Spacecraft and Rockets*, Vol. 4, No. 6, 1967, pp. 774–780. doi:10.2514/3.28950

[8] Capener E. L., Chown, J., Nanevicz, J. E., and Dickinson, L. A., "Studies on Ionization Phenomena Associated with Solid Propellant Rockets," *Solid Propellant Rocket Conference*, AIAA Paper 65-182, Washington, D.C., 1965.

[9] Ely, O. P., and Hockenberger R. W., "Rocket Exhaust Effect on Radio Frequency Transmission," *Journal of Spacecraft and Rockets*, Vol. 3, No. 3, 1966, pp. 310–314. doi:10.2514/3.28445

[10] Shimada, T., Daimon, Y., and Sekino, N., "Computational Fluid Dynamics of Multiphase Flow in Solid Rocket Motors," Japan Aerospace Exploration Agency, Rept. JAXA-SP-05-035E, 2006.

[11] Smoot, L. D., and Underwood, D. L., "Prediction of Microwave Attenuation Characteristic of Rocket Exhausts," *Journal of Spacecraft and Rockets*, Vol. 3, No. 3, 1966, pp. 302–309. doi:10.2514/3.28444

[12] Tevepaugh, J. A., Smith, S. D., and Penny, M. M., "Assessment of Analytical Techniques for Predicting Solid Propellant Exhaust Plumes," AIAA 10th Fluid and Plasmadynamics Conference, AIAA Paper 77-711, Albuquerque, NM, 1977.

[13] Smoot, L. D., Underwood, D. L., and Schroeder, R. G., "Prediction of Microwave Attenuation Characteristics of Rocket Exhausts," AIAA 6th Solid Propellant Rocket Conference, AIAA Paper 65-181, Washington, D.C., 1965.

[14] Lawton, J., and Weinberg, F. J., *Electrical Aspects of Combustion*, Clarendon Press, Oxford, 1969.

[15] Balwanz, W. W., and Weston, J. P., "The Prediction of Rocket Exhaust Interference with Radio Signals," Ions in Flames and Rocket Exhaust Conference, American Rocket Society, Paper 2591-62, Oct. 1962.

[16] Blevins, J. A., Frederick, R. A., Jr., and Coleman, H. W., "An Assessment of Microwave Measurement Techniques in Rocket Exhaust Applications," 32nd Aerospace Science Meeting & Exhibit, AIAA Paper 94-0671, 1994.

[17] Dash, S. M., Wolf, D. E., Beddini, R. A., and Pergament, H. S., "Analysis of Two-Phase Flow Processes in Rocket Exhaust Plumes," *Journal of Spacecraft and Rockets*, Vol. 22, No. 3, 1985, pp. 367–380. doi:10.2514/3.25758

I. Boyd
Associate Editor